Solid oxide fuel cells for shipping: A machine learning model for early detection of hazardous system deviations

Tomaso Vairo, Davide Cademartori, Davide Clematis, Maria Paola Carpanese, Bruno Fabiano [*]

DICCA – Civil, Chemical and Environmental Engineering Department - University of Genoa, Via Opera Pia, 15, 16145 Genoa, Italy

A B S T R A C T

With rising concerns about the amount of pollutant emissions generated by shipping and the consequent pressure to curb the environmental impact of shipping activities, fuel cells are expected to take an important role in ship propulsion. In particular, Solid Oxide Fuel Cells (SOFCs) are envisaged to provide high electrical efficiency and offer the opportunity of combining heat and power production. This work deals with the safety issues related to the safety implications of the use of Fuel Cells in maritime applications. A machine-learning model for identifying and intercepting critical events, based on the early detection of the system weak signals, is developed and applied to a Solid Oxide Fuel Cell (SOFC) system. The model relies on a hybrid approach: a data-driven model based on gradient-boosted decision trees and a computational model of the SOFC system are integrated to enhance the data-driven approach by implementing physics-based knowledge to boost the resulting predictive capabilities. The outlined approach even if it requires further validation at the full scale may be considered a step forward in enabling the prediction of the conditions that may lead to an accident with remarkable accuracy.

1. Introduction

Due to the well-spread environmental awareness and present-day energy instability, forced by external events, such as climate change and political crises, recent management and industrial remodelling directives are addressing the issue of the energy transition and the exploitation of new energy sources. The term "new energy transition" represents a pathway toward the transformation of the global energy sector from oil & gas to zero-carbon by the second half of this century. Within this broad context, the international legislation set by the IMO (International Maritime Organization) requires the reduction of greenhouse gases, SOx and NOx emissions from shipping (MEPC, 2011), thus stimulating a rising interest in the use of fuel cells for marine propulsion. Fuel cells are an excellent solution from an environmental perspective because they can operate with virtually no direct pollutant emissions, even when carbon-based fuels are used, with a high conversion efficiency, particularly at medium-low load, which is also where ships are most often operated during their lifetime (Baldi et al., 2020). Fuel cells are modular in nature and the intrinsic performance of a single cell is not different from a large stack. As a result, power production can be distributed over the ship without a penalty of increased fuel consumption, while electricity transport losses are reduced and redundancy is improved. For this reason, fuel cell systems are successfully applied in back-up power systems and data centers.

A variety of fuel cell types with distinct characteristics has been developed. The most relevant are:

- Low and High temperature Polymer Electrolyte Membrane Fuel Cells (LT/HT-PEMFCs),
- Phosphoric Acid Fuel Cell (PAFCs),
- Molten Carbonate Fuel Cells (MCFCs),
- Solid Oxide Fuel Cells (SOFCs).

As outlined in the work of Tronstad et al. (2017), the three most promising technologies for fuel cells marine use are LT-PEMFCs, HT-PEMFCs and SOFCs. Most of the working applications of fuel cells in shipping are related to the use of PEMFCs, due to the higher maturity of this technology. PEMFCs have been successfully used on submarines and tested for long periods on a passenger ferry. Table 1, adapted from Yuanting and Zengshi (2019), summarizes some of the most significant fuel cell experimental applications in shipping.

According to Van Biert et al. (2016), SOFCs can withstand the challenges of the maritime environment and be successfully employed for applications requiring tight limitations in volume and weight. SOFCs operate at high temperatures (between 500 and 1000 °C). Commonly,

---

* Corresponding author.
  E-mail address: brown@unige.it (B. Fabiano).

Nomenclature

Symbols

a	Exponential coefficient (-).
b	Exponential coefficient (-).
B	Permeability (m^2).
c	Exponential coefficient (-).
d_k	Diffusion driving force on species k (1/m).
D_{ik}	Binary diffusion coefficient of species i and k (m^2/s).
E_a^{act}	Activation energy for anodic reaction (kJ/mol).
E_c^{act}	Activation energy for cathodic reaction (kJ/mol).
E_{H_2/O_2}^{OCV}	Open circuit voltage (V).
E_{H_2/O_2}^{0}	Standard theoretical reversible voltage (V).
$E_{eq,i}$	Reversible voltage (V).
F	Faraday constant (C/mol).
i_a	Anodic current density (A/cm^2).
i_c	Cathodic current density (A/cm^2).
i_{a0}	Anodic exchange current density (A/cm^2).
i_{c0}	Cathodic exchange current density (A/cm^2).
i_ν	Volumetric current density (A/m^3).
J_i	Mass flux vector of species i, diffusion term (Kg/[m^2•s]).
M_i	Molar mass of species i (g/mol).
n	Number of electrons (-).
p_a	Anodic pressure (Pa).
p_c	Cathodic pressure (Pa).
$p_{,ref}$	Reference pressure (Pa).
Q_m	Volumetric mass source or sink (Kg/[m^3•s]).
R	Ideal gas constant (J/[mol•K]).
R_i	Mass source or sink of species i (Kg/s).
T	Operating temperature [K].
u	Velocity (m/s).
y_i	Molar fraction of species i (-).
Zreal	Real part of the impedance ($\Omega\ cm^2$).
Zimag	Imaginary part of the impedance ($\Omega\ cm^2$).

Greek Symbols

α	First transfer coefficient (-).
β	Second transfer coefficient (-).
γ_a	Anodic exchange current density coefficient.
γ_c	Cathodic exchange current density coefficient.
η	Overvoltage.
ξ	Friction factor (-).
λ	Lenght of triple phase boundaries sites ($\mu m\bullet\mu m^{-3}$).
ρ	Density (kg/m^3).
σ	Conductivity (S/m).
τ	Geometrical tortuosity (-).
φ	Voltage (V).
Φ	Porosity (-).
ω_i	Mass fraction of species i (-).

Subscripts and Superscripts

a	Anodic.
AFL	Anode Functional Layer.
c	Cathodic.
CFL	Cathode Functional Layer.
i,k	Species i,k.
in	Inlet.
l	Ionic.
m	Reaction m.
ν	Stoichiometric coefficient.
pore	Pore.
ref	Reference.
s	Electronic.
TPB	Triple Phase Boundary.
v	Volumetric.
O_2	Oxygen.
H_2	Hydrogen.
H_2O	Water.

the electrolyte is a thin dense layer of ceramic ionic conductors such as Yttrium Stabilized Zirconia (YSZ) and Gadolinium Doped Ceria (GDC). SOFCs usually feature a porous Ni-YSZ composite anode, while the porous cathode is normally made of Mixed Ionic Electronic Conductors (MIEC) such as Lanthanum Strontium Manganite (LSM), or Lanthanum Strontium Cobalt Ferrite (LSCF). These perovskites present good catalytic activity towards the Oxygen Reduction Reaction (ORR) and compatibility with conventional electrolytes. SOFCs are used in large-scale power production on shore, with capacities up to 10 MW and show flexibility towards different fuels such as direct methane (Chen et al., 2014), methanol (Liu et al., 2008) hydrogen, LNG and ethanol (Laosiripojana et al., 2007; Yang et al., 2020). Recently, also ammonia (NH_3) has attracted extensive attention because of its high hydrogen content and ease of liquidation under mild conditions. Notably, ammonia possesses one of the highest gravimetric hydrogen densities (17.8% w/w) with the highest volumetric hydrogen densities (0.107 kg-H_2 /L) (Valera-Medina et al., 2018) and new technologies for hydrogen production are currently investigated, e.g. by complete cracking. The employment of ammonia for clean energy can also be realized by producing the required hydrogen for energy production in fuel cells, as the ammonia is cracked by the anode within the cell and thus there is no need for a fore-line ammonia reformer (Lan and Tao, 2010). On these bases, generating clean electricity by ammonia attracted notable interest in the last decade intended to develop new automotive units, particularly because it can be directly fed to the SOFC fuel electrode (Wan et al., 2021). Additionally, ammonia has emerged as one of the likely front-runner fuels in the shipping industry's

decarbonization path, nevertheless, there are major safety issues that still need to be tackled, namely flammability, but particularly toxicity, especially when considering the possible application to cruise ships.

In industry, with the enforced standards, materials and competence available, hydrogen can be handled professionally, while in the sea transport sector, despite the potential of being widely applied, both for the power propulsion and ship energy supply, the high risks associated with its utilization still represent a major concern. Therefore, safety is one of the key issues that urgently needs to be solved in the design of a hydrogen fuel cell ship, as recently investigated in a work by Vairo et al. (2022), representing the starting basis for this research. As demonstrated in process plants, most significant potential for realizing a safe process is early in the development, via the introduction of process safety reviews throughout the design phase, including safety metrics in a dynamic process design (Bassani et al., 2023). In the marine application this is translated into an extension of the risk based design accounting for proper hazards and deviation consequences management. A peculiar case is connected to low-rate releases of light gases like H_2. In fact, an accidental release of flammable light gas can provoke a stratified gas cloud leading to two kinds of hazards: the first one refers to mechanical damage caused by overpressure resulting from an explosion, while the second one concerns heat exposure from fire development. Critical conditions for flash fire or explosion are rapidly reached in case of confined, or semi-confined spaces, thus requiring careful evaluation of the maximum admissible gas build-up (Palazzi et al., 2020). In this regard, the potential internal or external H_2 gas leakage scenario must be avoided during operation, as the decrease of the hydrogen partial

Table 1
Fuel Cell notable application in shipping.

Year	Nation	Vessel	Characteristics
2002	China	Fuyuan One	Fuel cell yacht: propulsion power 400 W, speed 7 km/h.
2005	China	Tianxiang One	Experiment ship: propulsion power 2 kW, speed 7 km/h ca.
2007	EU	ZEMships	The world's first Zero Emissions Ships project for a commercial passenger ship. The 100-passenger capacity ship has a hybrid propulsion mode and integrates two hydrogen fuel cells with a peak power of 48 kW and 560 V lead-acid batteries.
2008	Germany	Alsterwasser	The 100-passenger capacity "Alsterwasser" hydrogen fuel cell cruise ship was developed. The ship can produce a power of 100 kW and reaches a maximum speed of 14 km/h. Since its introduction, "Alsterwasser" has transported more than 14,000 passengers.
2009	NL	Fuel Cell Boat Amsterdam	A 100-passenger capacity for canal tourism in Amsterdam. The ship is equipped with a 60–70 kW hydrogen fuel cell system, based on high-pressure hydrogen with a cruising range of 9 h at a speed of 7 knots.
2009	Norway	Viking Lady	Viking Lady is the vessel passed the marine fuel cell certification of DNV. The hydrogen fuel cell system power is 320 kW and the fuel is liquefied natural gas. It was the first operational hydrogen fuel cell ship globally.
2017	France	Energy Observer	A hydrogen–wind–sunlight-powered ship. The ship characterized by length and weight of 30 m and 20 t respectively, and a 22 kW hydrogen fuel cell system.
2022	Japan	Yomiuri Shimbun	A fishing vessel equipped with 450 L of hydrogen fuel, speed of up to 37 km/h.

pressure not only reduces the fuel efficiency (increasing the gas conversion resistance) but might also trigger the explosion scenario. This risk is well relevant due to its physical and chemical hazards, e.g., the rather wide explosion region, low ignition energy and high burning velocity, thoroughly and critically explored in the work by Rigas and Amyotte (2012), to which the reader is addressed for further insights.

In the explored sector, the effective identification of weak signals may allow recognizing accident precursors, i.e. "the conditions, events and sequences that precede and lead up to an accident" (NAE, 2004). It is worth noting that if minor deviations or weak signals are timely identified and proactively managed, the scenario evolution can be stopped: a recent investigation by Pasman (2020) provided notable case-studies where weak signals were recognized on the work floor, but top management failed to act upon them. In the considered application, even though the thin electrolyte between the SOFCs electrodes is manufactured to be as much dense as possible, cell degradation or mechanical failure occurring in the sealant might give rise to small cracks which enable the internal H_2 crossover (Chen et al., 2016; Wang et al., 2020). Rasmussen et al. (2008) described in their work the development of an experimental method to pinpoint gas leakage, while a theoretical approach represents a challenging research topic. The internal gas leak through the electrolyte was quantified under different conditions, as was the external leak from the surroundings to the anode. The internal gas leak did not depend on the pressure difference between the anode and the cathode gas compartments and can thus be described as diffusion driven. External leaks between the surroundings and the anode, but not on the cathode were observed. They were influenced by the pressure difference and are thus driven by both concentration and pressure gradients.

Jia et al. (2017) enhanced the gas leakage calculation method by resorting to Electrochemical Impedance Spectroscopy (EIS) and Distribution of Relaxation Time (DRT) analyses to investigate the electrochemical performance of the cell. EIS employs a frequency response analyzer to apply either a small AC voltage or current perturbation signal to a cell and measures its output response in a wide frequency range. The impedance is calculated as the ratio between the voltage and the current, expressed as phasors, in a selected frequency range after applying a small sinusoidal perturbation. This characterization technique enables the evaluation of the electrochemical performance of SOFCs and the identification of their major weak points. EIS, DRT and Equivalent Circuit (EC) models are often combined to quantify the impedance of these systems, finding and matching the time constants of the characteristics resistive contributions.

Following the reasoning of Yua et al. (2022), we restricted weak early signals to those deviations that can be considered as precursors, i. e., conditions that could warn for adverse events. Currently, a large interest from the scientific community is growing towards the application of Machine Learning (ML) algorithms for the assessment of systems safety. To enhance a new safety paradigm, researchers implemented novel algorithms for the different aims of predicting, analyzing and diagnosing deviations within safety, risk, sustainability and accident applications in various domains. A wide number of intelligent algorithms can categorize and analyze plant deviations and support making informed decisions. Renewable energy systems powered by Artificial intelligence (AI) techniques can provide a functional contribution to optimizing the operational control modalities of the systems and improving the overall operational effectiveness (Al-Othman et al., 2022). Novel and improved methods for early warning, prediction of actual risk and safety warranty, both from a design point of view and in the dynamic should be based on a critical and balanced application of new developments in data science and digital technology with fundamentals science and engineering principles (Pasman et al., 2021). ML based prediction model of hazardous failures of pipelines was explored considering corrosion at high CO_2 partial pressure by Abbas et al. (2018) and considering fault detection modelling for submarine layout by Eastvedt et al. (2022). A detailed evaluation concerning energy consumption dependability on different features of a complete wastewater treatment plant was developed by Bagherzadeh et al. (2021). An accurate critical review of literature on hazardous events and supervised machine learning algorithms including algorithm actual field applications degree of success and limitations in a peculiar sector is provided by Osarogiagbon et al. (2021) and we refer the reader to the references quoted therein The need for research on Artificial Intelligence (AI) /ML in fuel cells systems is pointed out by Li et al. (2018). There are several applicative research activities on the use of ML algorithms for safety assessment in shipping, related to the energy transition, relying on the basic assumption that a good algorithm should allow for quick, accurate, and reproducible convergence. Vairo et al. (2021) developed a Bayesian inference-based approach, adopting the Baum-Welch Hidden Markov Model (BW-HMM) formulation, verifying its reliable predictive capabilities in LNG bunkering operation. The application of Artificial Neural Networks (ANN) to estimate the pressure drop in a PEMFC is presented by Pei et al. (2016), while different approaches mainly related to Kernel methods and Principal Component Analysis (PCA) are critically discussed by Petrone et al. (2013) and Zheng et al. (2013).

The main issue related to the use of pure data-driven models for safety assessment is that calculations and physical laws are uncoupled. Commonly, the relationship between inputs and outputs is physically defined but calculations only rely on massive experimental datasets. Therefore, the nonlinear relationship between inputs and output is trained in a black box. The model-based approaches, like Bayesian Networks (BN) and HMM ones, are explainable by definition. However, probabilistic models, which are essentially extensions of Expectation Maximization (EM) algorithms, hold the risk of converging on locally optima solutions thus requiring an accurate and extensive training process. Physics-informed Machine Learning models are gaining momentum, as they can be trained from additional information obtained by enforcing the physical laws. Such physics-informed learners integrate

data and mathematical models, implementing them through neural networks, kernel-based regression networks, or tree-based models (Em Karniadakis et al., 2021).

Hydrogen fuel cells have the potential to revolutionize the maritime industry as a cleaner and more sustainable alternative energy source. However, to ensure safe and reliable operation of hydrogen-powered vessels, it is essential performing in-depth risk assessments to identify, mitigate and mange hazards, adapting the technology to the marine environment and its safety under variable conditions. Accordingly, the design of the ship of the future implies an adaptation of present prescriptive regulations, to be realized according to a risk-based approval approach. To help addressing these needs, this paper presents a dynamic risk assessment combined model, conceived to identify the precursors of hydrogen internal leakage in fuel cell systems. A physics-informed gradient-boosted tree model is proposed to predict the behavior of an operating SOFC, focusing on weak signals suitable to anticipate internal hydrogen leakage conditions. The remainder of this paper is as follows: Section 2 outlines the designed research workflow and applied material and methods; Section 3 details the modelling steps and Section 4 presents the results. Conclusions are drawn in Section 5, highlighting as well current limitations and perspectives for further research opportunities.

2. Material and methods

According to the logical flow diagram of the overall study depicted in Fig. 1, this section presents all materials and methods used for addressing the research, including the numerical model, the data driven model and the safety assessment methodology.

2.1. CFD Modelling

The electrochemical performance of SOFCs can be simulated by means of computational tools. The construction and validation of a Computational Fluid Dynamic (CFD) model enable the fast generation of several electrochemical data in different operating conditions both in stationary and transient mode. This physical-based approach speeds up
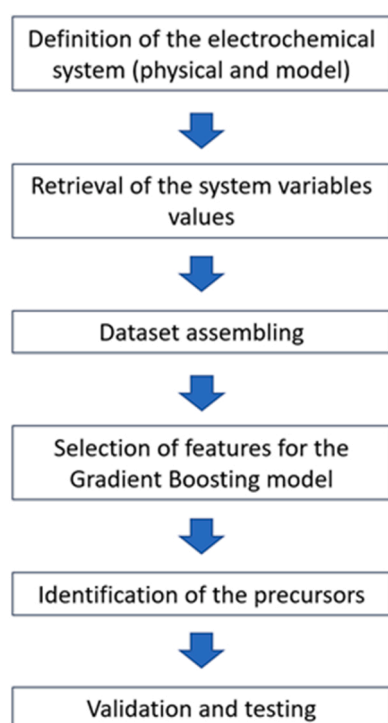

Fig. 1. Flow diagram of the research study.

the data acquiring process and generates large datasets, which can be used for ML algorithm training.

With the purpose of benefitting from electrochemical data simulated under different conditions, we built up a CFD model for a conventional circular button cell, featuring the electrochemical properties of the ceramic materials included in the commercial cell tested experimentally, as summarized in Table 2. The button SOFC is a conventional fuel electrode-supported cell, whose different layers are shaped by the tape casting and screen-printing techniques, starting from suspensions including the ceramic powders and organic additives (solvent, dispersant, binder, plasticizers etc.). During its manufacturing, the sample undergoes thermal treatments at different operating temperatures in order to achieve the full densification of the electrolyte material and the electrode solid phases. The high operating temperature of the sintering process ($>1000\ °C$) also promotes the burn out of the organic pore formers which are commonly added in the starting solutions of the electrodes to shape the gas channels for fuel and air diffusion. The electrochemical investigations on button SOFCs provide insightful information over the cell performance and the impact of the main resistive processes which hinder power production. Therefore, both the analysis of the kinetics of the electroreduction/oxidation processes and the in-depth investigation of the button cells microstructural properties are the starting steps for the development of a high-performing SOFC. Additionally, once the electrochemical performance of a cell holding a low-size active area ($1–2\ cm^2$) is validated in terms of electrochemical performance and stability over time, its architecture does not change in the subsequent upscaling process whose main focuses are the production of large-size cells and the effective design of the final stack for power production. Therefore, the findings obtained from the analysis of EIS data of button SOFCs can be effectively employed to analyze the electrochemical behavior of larger cells holding the same architecture.

A button SOFC was tested and analyzed by EIS in fuel cell mode, thus producing electrical power when fed with fuel (humid hydrogen, H_2: H_2O - 0.97:0.03) and air (O_2:N_2 – 0.21:0.79) at ambient pressure. The electrochemical investigations were carried out in a high temperature vertical test rig, ProboStat™ (NorECs AS, Norway), placing metallic meshes of Ni and Pt acting as current collectors over the surface of the anode and the cathode to ensure a homogeneous current distribution during EIS analyses and good electrical contact between the platinum wires connected to the potentiostat (PGSTAT302N from Autolab, METROHM) and the cell. Owing to the circular cell symmetry, the 2D model is axially symmetric and simulates the electrochemical performance in fuel cell operating mode at 750 °C.

2.1.1. Electrochemical model

The electrochemical model defines the reaction rate and transport mechanism of the species in the cell and gas channels utilizing steady-state conservation equations. As a working hypothesis, the simplified approach includes only H_2 as fuel participating to the electrochemical reaction, according to Eq. 1 and 2.

$$O_2 + 4e^- \leftrightarrow 2O^{2-} \tag{1}$$

$$2H_2 + 2O^{2-} \leftrightarrow 2H_2O + 4e^- \tag{2}$$

The Open Circuit Voltage, OCV, is described by:

Table 2
Materials and geometrical dimensions of the simulated button SOFC.

Layer	Material	Thickness (µm)	Diameter (mm)
Anode Substrate	Ni-YSZ	240	24
Anode Functional Layer	Ni-YSZ	30	24
Electrolyte	8YSZ	8	24
Cathode	LSCF-GDC10	50	12

$$E_{H_2/O_2}^{OCV} = E_{H_2/O_2}^0 - \frac{RT}{2F} \ln\left(\frac{y_{H_2O,in}}{y_{H_2,in}\sqrt{y_{O_2,in}}}\right) \tag{3}$$

The standard theoretical reversible voltage, depending on the operating temperature T, is calculated according to:

$$E_{H_2/O_2}^0 = 1.253 - 2.4516 \bullet 10^{-4} \bullet T \tag{4}$$

The general reversible voltage can be separated into anode and cathode contributions as follows:

$$E_{eq,i} = E_{H_2/O_2}^0 - \frac{RT}{nF} \ln\prod_j \left(\frac{p_j}{p_{j,ref}}\right)^{\nu_j} \tag{5}$$

The overpotential can then be divided into the anode and cathode one as follows:

$$\eta_a = \varphi_s - \varphi_l - E_{eq,H_2} \tag{6}$$

$$\eta_c = \varphi_s - \varphi_l - E_{eq,O_2} \tag{7}$$

The concentration overvoltage is calculated as:

$$\eta_{conc,a} = \frac{RT}{2F} \ln\left(\frac{y_{H_2O,TPB} \bullet y_{H_2,in}}{y_{H_2,TPB} \bullet y_{H_2O,in}}\right) \tag{8}$$

$$\eta_{conc,c} = \frac{RT}{4F} \ln\left(\frac{y_{O_2,in}}{y_{O_2,TPB}}\right) \tag{9}$$

The governing equations for ion and electron transport in their corresponding conducting phases follow the Ohm's law and are described by:

$$\nabla \bullet (-\sigma_l \nabla \varphi_l) = i_{v,l} \tag{10}$$

$$\nabla \bullet (-\sigma_s \nabla \varphi_s) = i_{v,s} \tag{11}$$

The kinetic expressions implemented in the present model for the evaluation of the local current densities were developed starting from Yahya et al. (2018) and Mozdzierz et al. (2019), who in their works proposed a model tuned on commercial cells featuring the same ceramic materials.

The kinetic laws rely on the standard Butler-Volmer expression, and the exchange current densities can be calculated in the general form:

$$i_{a0} = \gamma_a \bullet \left(\frac{p_a y_{H_2}}{p_{,ref}}\right)^a \bullet \left(\frac{p_a y_{H_2O}}{p_{,ref}}\right)^b \bullet \exp\left(-\frac{E_a^{act}}{R}\right) \tag{12}$$

$$i_{c0} = \gamma_c \bullet \left(\frac{p_c y_{O_2}}{p_{,ref}}\right)^c \bullet \exp\left(-\frac{E_a^{act}}{R}\right) \tag{13}$$

2.1.2. Microstructural Model

The microstructural parameters of the simulated cell were retrieved by an accurate literature review (Bertei et al., 2014; Mozdzierz et al., 2019; Yahya et al., 2018) and implemented into the model, to simulate the gases diffusion within the electrodes porous channels.

Table 3 summarizes the main morphological parameters set in the model.

Table 3
Microstructural parameters of the electrodes.

Parameter	Value	Unit
B_{CFL}	$8 \bullet 10^{-15}$	m^2
B_{AFL}	$1.1 \bullet 10^{-15}$	m^2
Φ_{CFL}	0.39	-
Φ_{AFL}	0.26	-
$\tau_{factor, AFL}$	4.51	-
$\tau_{factor, CFL}$	2.4	-
$d_{pore,CFL}$	1.02	μm
$d_{pore,AFL}$	0.71	μm

2.1.3. Momentum conservation

The reference expressions for momentum are based on the Navier-Stokes equations for the gas flow channels, while the Brinkman equations have been adopted to describe the flow within the gas diffusion channels inside the electrodes. The basic hypotheses the model is built upon are incompressible flow and no volume forces exerted on the fluid.

Mass and momentum conservation can be conveniently described as follows:

$$\rho\nabla \bullet u = Q_m \tag{14}$$

$$\frac{1}{\Phi}\rho(u \bullet \nabla)u\frac{1}{\Phi} = \nabla[-pI + K] - \left(\frac{\mu}{B} + \rho\beta u + \frac{Q_m}{\Phi^2}\right)u \tag{15}$$

The mixture viscosity of the gas phase is calculated on the basis of the kinetic theory expressed by Brokaw (1965). The mass source term is described by the Faraday equation:

$$Q_m = \sum_m\sum_i \frac{\nu_i i_\nu}{n_e F}M_i \tag{16}$$

2.1.4. Species transport

Advection and diffusion take place in the gas flow channels and in the porous electrode and are responsible for the species transport. In stationary conditions, the mass conservation equation reduces to:

$$\rho(u \bullet \nabla)\omega_i = -\nabla \bullet J_i + R_i \tag{17}$$

The mass source term R_i is calculated via the Faraday's law while J_i represents the diffusion term that is expressed throughout the Maxwell-Stefan diffusion model:

$$J_i = -\rho\omega_i\sum_k D_{ik}d_k \tag{18}$$

The diffusion coefficients D_{ik} are calculated according to the Fuller model (Fuller et al., 1966):

$$D_{H2/H2O} = \frac{0.0143T^{1.75}}{p_a\left(6.12^{0.33} + 13.1^{0.33}\right)^2}\sqrt{\frac{\frac{1}{M_{H2}} + \frac{1}{M_{H2O}}}{2000}} \tag{19}$$

$$D_{H2/H2O} = \frac{0.0143T^{1.75}}{p_c\left(16.3^{0.33} + 18.5^{0.33}\right)^2}\sqrt{\frac{\frac{1}{M_{O2}} + \frac{1}{M_{N2}}}{2000}} \tag{20}$$

The diffusion drag force of species i on species j is provided by:

$$d_k = \nabla x_j + \frac{1}{p}\left[(x_j - \omega_j)\nabla p\right] \tag{21}$$

2.1.5. Boundary conditions and assumptions

The operating temperature for the whole set of simulations was maintained at 750 °C to perform an effective electrochemical comparison with the I-V curve obtained from the experimental tests. The inlet molar fuel composition was set to a ratio H$_2$:H$_2$O corresponding to 0.99:0.01, while the inlet composition of the air flow channel was maintained at a ratio O$_2$:N$_2$ equal to 0.21:0.79. The inlet fluxes for the fuel and air flow channels were adjusted to 0.016 Nl min^{-1} cm^{-2} and 0.04 Nl min^{-1} cm^{-2}. At the inlet and outlet boundaries, the model does not include any relative pressure change. The remaining surfaces are set as no-slip wall conditions and the inlet gases flow normally to the anode and cathode surfaces to achieve a homogenous distribution of the reactants over the electrodes. The Finite Element Method (FEM) is employed to solve numerically the set of governing Partial Differential Equations (PDEs).

2.2. The ML model

Gradient Boosting (GB) is a machine learning algorithm, used for both classification and regression problems, starting from the principle

that many weak learners (e.g. shallow trees) can provide an accurate predictor. A weak hypothesis, or weak learner, can be defined as one learner whose performance is at least slightly better than a random chance. As amply known, gradient boosting involves three elements:

1. a loss function to be optimized;
2. a weak learner to make predictions;
3. an additive model to add weak learners to minimize the loss function.

The loss function must be differentiable, but many standard loss functions can be used, depending on the application. Decision trees are used as the weak learner in gradient boosting. Specifically, regression trees are used that output real values for splits and whose output can be added together, allowing subsequent models outputs to be added and correct the residuals in the predictions. A gradient descent procedure is used to minimize the loss when adding trees. Gradient descent is used to minimize a set of parameters; after calculating the error, the parameters are updated to minimize that error, moving in the right direction by reducing the residual loss.

The first step in gradient boosting is to build up a base model to predict the observations in the training dataset. The procedure can be conveniently described by Eqs. (22), (23) and (24).

$$F_0(x) = argmin_\gamma \sum_{i=1}^{n} L(y_i, \gamma) \tag{22}$$

where L is the loss function, γ is the predicted value, and argmin (*argument of the minimum*) corresponds to the set of values where the loss function attains the minimum.

The loss function is expressed by Eq. (23).

$$L = \frac{1}{n} \sum_{i=0}^{n} (y_i - \gamma_i)^2 \tag{23}$$

where y_i is the observed value and γ_i is the predicted value.

The target is to find a value of gamma, which minimizes the loss function. The algorithm differentiates the loss function and set it equal to zero, as shown in Eq. (24).

$$\frac{dL}{d\gamma} = -\sum_{i=0}^{n} (y_i - \gamma_i) \tag{24}$$

The next step is to calculate the pseudo residuals, which are intermediate error terms, i.e. difference between the actual value and intermediate predicted value, according to Eqs. (25) and (26).

$$r_{im} = -\left[\frac{\delta L(y_i, F(x_i))}{\delta F(x_i)} \right]_{F(x)=F_{m-1}(x)} \quad for\ i = 1, \ldots, n \tag{25}$$

where $F(x_i)$ is the previous model and m is the number of trees made.

The derivative of loss function, with reference to the predicted value, is:

$$\frac{\delta L}{\delta \gamma} = -(y_i - \gamma_i) \tag{26}$$

In the formula of residuals, Eq. (26), the predicted value is the prediction performed by the previous model.

In the next step, a model on the pseudo residuals is built, and predictions are made. The goal is to minimize these residuals and minimizing the residuals will improve the model accuracy and prediction power. Therefore, using the residuals as targets, it is possible to generate new predictions. The predictions, in this case, will be the error values, not the predicted values since the new target column represents the error.

Thus, $h_m(x)$, i.e. the decision tree, is obtained on the basis on these residuals.

The output values for each leaf of the decision tree are subsequently obtained according to Eq. (27).

$$\gamma_m = argmin_\gamma \sum_{i=1}^{n} L(y_i, F_{m-1}(x_i) + \gamma h_m(x_i)) \tag{27}$$

where $h_m(x_i)$ is the decision tree made on residuals and m is the number of trees.

The output value for the leaf is the value of γ that minimizes the Loss function. The left-hand side γ is the output value of a particular leaf. On the right-hand side $[F_{m-1}(x_i) + \gamma h_m(x_i)]$ is the repetition of the first step, but here the previous predictions are taken whereas earlier there was no previous prediction.

Analogously, when applying the gradient boosting classification, the loss function is calculated according to Eq. (28).

$$L = -\sum_{i=1}^{n} y_i \log(\gamma) + (1-\gamma)\log(1-\gamma) \tag{28}$$

The predictive model is based on gradient-boosted trees and the algorithm described in Section 2.2.

The overall logical architecture of the complete predictive model is depicted in Fig. 2.

The training data for the ML model are obtained by the construction of a calibrated CFD model for a circular button SOFC that simulates the Nyquist plots of the system under normal operating conditions and according to the potential internal H_2 leakage scenario.

2.3. Safety assessment

For hydrogen fuel cell vessels, no dedicated class rules exist (Aarskog et al., 2020). Hence, the design approach described in the International Code of Safety for Ships Using Gases or Other Low-flashpoint Fuels (IMO, 2017) must be applied. The main IGF-code requirements are:

- safety of the fuel systems must be equivalent to that achieved with new and comparable conventional oil-fueled main and auxiliary machinery;
- a risk assessment must be performed to assess risks arising from the alternative design;
- an explosion assessment must be performed;
- consequences from one event shall remain local and not escalate to other parts of the vessel, or threaten ship stability.

By the means of a standard Quantitative Risk Assessment (QRA), it is possible to define and apply design principles and technical measures both preventing and mitigating the risk.

The main issues identified in the fuel cell power-system risk assessment are summarized as follows (Alvestad and Berge, 2021):

- strong exothermic reaction of reformer material;
- internal leakage in Fuel Cell Module;
- high energy collision with the potential to penetrate a Liquid Hydrogen tank;
- rupture of CH_2 tank containment system;
- leakage of hydrogen gases;
- failure of fuel pressure reduction;
- failure of the electrical power output conditioning system;
- thermal runaway of onboard energy buffer;
- loss of the inert gas system.

The QRA and related mitigation measures are effective in identifying and handling the risks associated with H_2 loss of containment, but not so effective with fuel cell system-specific risks, such as the internal leakage in fuel cell module, which is the specific topic addressed in this paper. As anticipated, cracking of fuel cell plates may cause internal leakages, leading to high stack temperatures, internal oxidation processes and
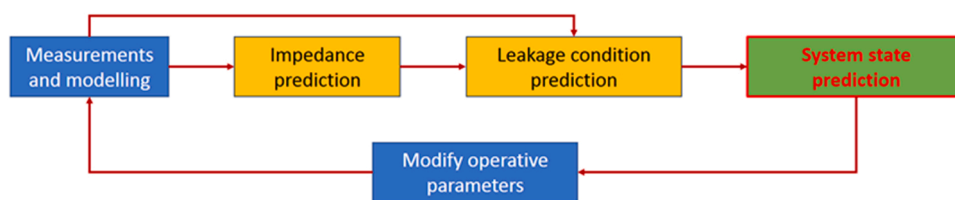
Fig. 2. Predictive model logical architecture.

internal fire.

3. Modelling

3.1. Physical model

The validation of the CFD model was performed by fitting the experimental data of the current-voltage characteristic of a conventional button cell. The simulated data were obtained by the implementation of the electrochemical parameters retrieved from the literature (Bertei et al., 2014; Mozdzierz et al., 2019; Yahya et al., 2018), in the computational code. The model was validated by adjusting the kinetics parameters without modifying the microstructural ones, with the purpose of minimizing the root mean square error between the experimental and simulated data. The optimized set of free variables data is summarized in Table 4. Fig. 3 provides the comparison between experimental and simulated I-V curves evidencing a fairly good agreement reflected by a calculated mean error corresponding to 3%.

The CFD model was employed as well for the purpose of simulating the impedance spectra at different oxygen partial pressures. In particular, the internal leakage of hydrogen was simulated by the reduction of the oxygen partial pressure at the cathode. The potential penetration of hydrogen through the electrolyte would lead, indeed, to the decrease of pO_2 and pN_2. A potential explosive scenario is reached if the p_{H2} overcomes the LEL of the H_2-air mixture. The SOFC operating conditions affect the extension of the explosion limits because if temperature is increased, LEL is shifted to lower H_2 concentrations, while if the system works over pressurization, LEL increases with increasing initial pressure. For this work, considering the cell operative conditions corresponding to 750 °C and the atmospheric pressure and applying a conservative approach, 1 mol% of H_2 was set as reference partial pressure for the given risk scenario.

The impedance spectra were simulated in the frequency range between 1 MHz and 0.1 Hz, recording 12 points for frequency decade and applying a sinusoidal perturbation of 10 mV. The Nyquist plots were measured in different operating points (1 V, 0.8 V and 0.65 V) thus obtaining at standard operating conditions (0.21 O_2, 0.79 N_2) the results visualized in Fig. 4. Analogously, Fig. 5 shows the impedance of the cell in the simulated risk scenario.

It stands to reason that the correlation between intrinsic properties and electrochemical performance can be effectively identified if CFD models are properly calibrated with reproducible electrochemical
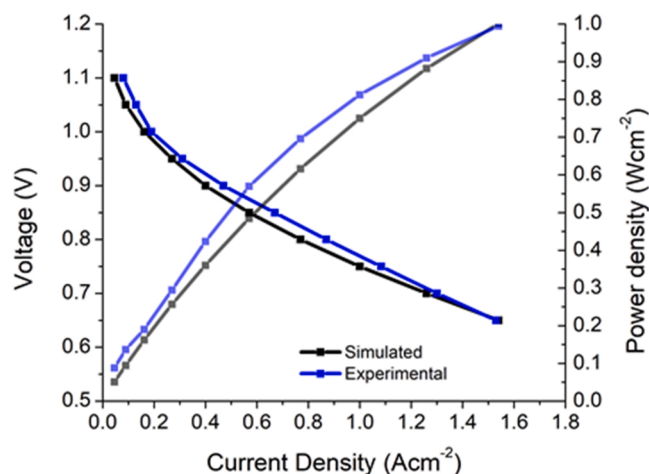

Fig. 3. Experimental and Simulated I-V and I-P characteristics.
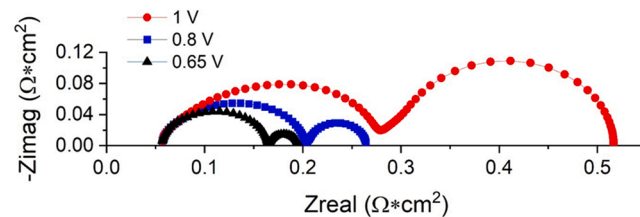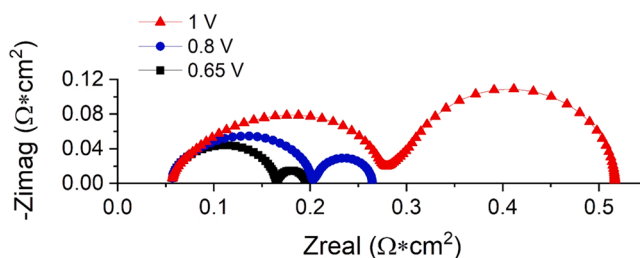

Fig. 4. Nyquist plots at different operating voltage in standard conditions.

Fig. 5. Nyquist plots at different operating voltage simulating 1% mol H_2 in the air electrode compartment.

experimental data and then verified in different electrode microstructures. However, electrochemical models are commonly calibrated by adjusting microstructural and/or kinetics parameters just on a single set of I-V characteristics without evaluating their validity in different samples, or operating conditions (see e.g. Janardhanan al, 2007; Jiang et al., 2003). EIS data hold more information than polarization curves and, especially when integrated with DRT and EC modelling, they can break down the different physical processes according to their characteristic timescale, thus providing a more comprehensive tool for the validation of electrochemical models (Asensio et al., 2021; Carpanese et al., 2017; Clematis et al., 2019). The authors acknowledge that the

Table 4
Optimized set of data for the minimization of the root mean square error between the simulated and experimental I-V curve.

Parameter	Optimized Value	Unit
γ_a	1.2×10^9	A/m^2
γ_C	1×10^9	A/m^2
a	1	-
b	1	-
c	0.25	-
E_a^{act}	120	kJ/mol
E_c^{act}	100	kJ/mol
$\lambda_{TPB, CFL}$	2.11	m/m^3
$\lambda_{TPB, AFL}$	4.44	m/m^3

validation of the simulated impedance spectra agianst the experimental ones should be performed firstly validating the sub-models describing the physical processes which occur within the electrochemical cells (ions migration, charge transfer, gas diffusion), depicted in Fig. 6. In other words, even though a model is calibrated to fit the experimental IV curves, the actual contribution to the overall polarization resistance might not be precisely identified by the physical based expression, which are implemented in the code. The different physical processes, which are responsible for the main resistive contributions (charge transfer, diffusion, gas conversion…), cannot be properly deconvoluted if the impedance of the system is described by physical expressions, which resort to general exponential factors.

In particular, even though the physical based law used in this work to express the exchange current density dependencies is well accepted to describe the relation between current and species partial pressure when there is no available electrical path (Ferrero et al., 2015), the γ parameter approximates all the kinetic steps (species adsorption, surface diffusion, charge transfer…), which experimentally could be deconvoluted by the combination of EIS, DRT and EC. Thus, in order to validate the simulated EIS spectra, additional in-depth calibrating studies should be carried out to adjust the physical-based parameters of the model to the behavior of the samples under investigation.

The EIS data generated in this work translate the potential risky scenario in an overall decrease of the cell performance due to the lower pO_2 at the cathode and penalized H_2 gas conversion at the anode. These two physical phenomena are both registered in the different sets of the simulated impedance data, which are subsequently employed for the training of the ML algorithm. Therefore, the purpose of the simulations of this paper is not the validation with correspondent experimental EIS data (which would require a large number of experimental analyses), but rather, the generation of impedance datasets which are physically representative of the different operating conditions. The approach followed in this work can be upgraded and applied to experimental cells if long-experienced SOFC manufacturing companies and research groups use and share validated kinetics laws for the CFD simulations of their systems.

3.2. Data-driven model

In order to obtain a reliable prediction of critical values, the measured and calculated data are integrated into the Data driven model, schematized in the above-mentioned Fig. 2, following the reasoning outlined in Section 2. The impedance (real and imaginary part), and the current density were determined in different operating conditions. Each condition may lead to an internal leakage or not, depending on the feature combination. The predictive capability of the data driven framework was tested in two different configurations. The first predictive model does not contain any information on physics so, according to Jia et al. (2017), it allows determining the state of the system based on the impedance value. Table 5 summarizes the head of the first training dataset, containing 4392 rows.

The second model relies on physical information related to the
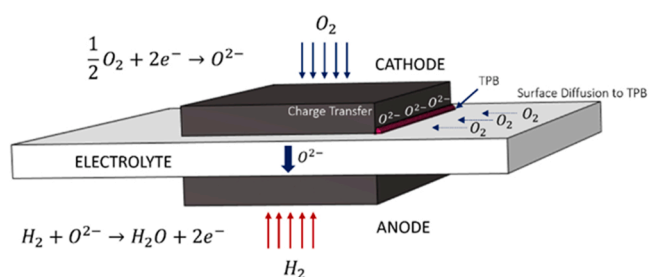
Table 5
Head of the first dataset utilized in the training step.

Frequency (Hz)	Z real (Ω cm^2)	Z imaginary (Ω cm^2)	State
100000	0.154936	0.027114	leak
82540.42	0.157857	0.023723	leak
68129.21	0.160156	0.020526	safe
56234.13	0.161926	0.017594	safe
100000	0.170397	0.050316	safe

current density (i-V curves) obtained both from the second dataset (measured data by experimental runs) and calculated data (based on the developed mathematical model).

The added physical information is the working point of the cell, i.e. the current-voltage couple at which the impedance is registered. The relation between impedance and I-V characteristic is given by:

$$Z = \frac{d\eta}{di} \tag{29}$$

By definition, Area Specific Resistance, ASR, is provided by:

$$ASR = \frac{\sum \eta_k}{i} = \frac{OCV - E_{cell}}{i} \tag{30}$$

where OCV is the open circuit voltage. The impedance Z of the cell can thus be identified either as the local slope around the working point in the I-V curve, or as the Z_{real} in the Nyquist plot.

Table 6 provides a summary of the head of the second dataset.

4. Results and discussion

As shown in Table 7, following the training step, the first model is fed with the impedance related features, being the final target represented by the "State" label reported in the last column.

It must be underlined that a portion of the dataset corresponding to 20% is kept for testing the model performance and the remaining 80% is used for training and validation. The predictive ability of the model is thoroughly analyzed by considering the metrics detailed in the following (Ke et al., 2017).

- The bias-variance tradeoff (i.e. metric during training), whose meaning is to check the presence of overfitting by comparing the training error and the validation error. Fig. 7 depicts the obtained results, where the label "training" identifies the error trend during the training phase of the model, i.e. how much the model is learning from the input data, while the label "valid_0″ represents the error during the validation phase.
- In order to evaluate the predictive capability, Table 8 summarizes the F-1 score calculated according to the precision and recall of the test. By definition, "precision" is the number of true positive results divided by the number of all positive results, including those not identified correctly, and "recall" is the number of true positive results divided by the number of all samples that should have been identified as positive.
- The confusion matrix reproduced in Fig. 8 allows the immediate visualization of the performance of the algorithm, by an ad-hoc graphical layout. Each row of the matrix represents the instances

Fig. 6. Schematic of some of the physical steps taking place during electrochemical operation in a SOFC.

Table 6
Head of the second dataset.

V	A	Frequency	Z real (Ω cm^2)	Z imaginary (Ω cm^2)	State
0.65	1.482203	100000	0.154936	0.027114	leak
0.65	1.556673	82540.42	0.157857	0.023723	leak
0.65	1.796067	68129.21	0.160156	0.020526	safe
0.8	1.482203	56234.13	0.161926	0.017594	safe
1	0.794351	100000	0.170397	0.050316	safe

Table 7

Input features of the first model and target label.

Frequency (Hz)	Z real (Ω cm²)	Z imaginary (Ω cm²)	State
100000	0.154936	0.027114	leak
82540.42	0.157857	0.023723	leak
68129.21	0.160156	0.020526	safe
56234.13	0.161926	0.017594	safe
100000	0.170397	0.050316	safe

Fig. 7. Errors in training and validation for the first model.

Table 8

First model F-1 score.

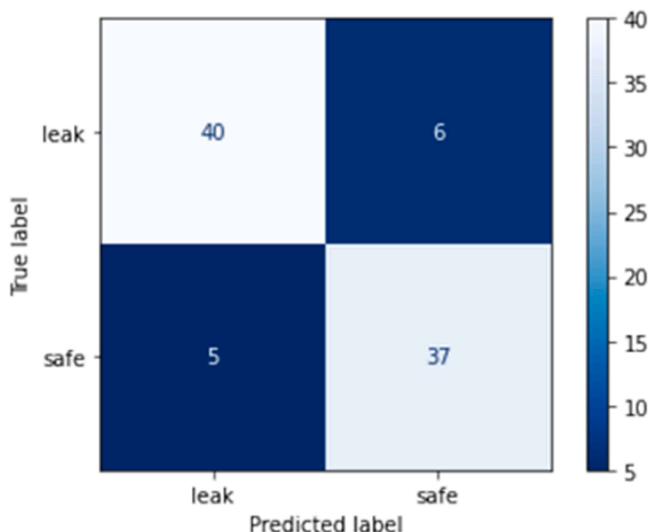|	Precision	Recall	F-1 score	Support
Leak	0.89	0.85	0.87	79
Safe	0.83	0.88	0.85	66
Accuracy			0.86	145
Macro avg.	0.86	0.86	0.86	145
Weighted avg.	0.86	0.86	0.86	145

Fig. 8. First model confusion matrix.

in an actual class, while each column represents the instances in a predicted class.

Results evidence that the predictive ability of the first model is fairly satisfactory, attaining an F-1 score corresponding to 0.86. Although the

adopted algorithm exhibits a tendence towards overfitting, the validation error trend shows that the performance of the model could improve with more data. Nevertheless, the presence of false positives can create a security flaw, so the first model cannot be considered completely reliable. On these grounds, the fed for the second model was conveniently modified, inserting the i-V data, as described in Section 3.2.

The input features of the second model are summarized in Table 9, where the target column is the same of Table 7.

The performance of the refined model is evaluated with the same approach. The training metric is reproduced in Fig. 9, the F-1 score is summarized in Table 10, and the corresponding confusion matrix is depicted in Fig. 10.

The performance of the physics-refined model exhibits a sharp increase. The impact of the new information is evident by analyzing the predictive accuracy, as presented in Table 10.

The feature importance, shown in Fig. 11, evidences the relevance of the new added feature. In Fig. 11, X-axis refers to techniques that calculate a score for all the input features for a given model, being the scores a quantitative estimate of the sensitivity of each feature. A higher score means that the specific feature will have a larger effect on the model that is being used to predict a certain variable. Feature Importance is useful for interpreting the model. By calculating the scores for each feature, it is possible to determine which features attribute the most to the predictive power of your model. The feature importance is calculated based on the mean decrease in impurity, which measures how effective each feature is at reducing uncertainty, by counting how many times the nodes split on the feature. The basic assumption is that the more important the feature is, the more times it is split.

Results evidence that the improved model relying on the new information (current density) as the best predictor, associated with the impedance data, as the most appropriate precursor, is fully consistent with the actual physics of the analyzed phenomenon. Upon proper further validation, the modelling framework can be very powerful in the management of risk situations in the day by day operation of fuel cell applications, provided that the network training is accurately developed during the design stage.

5. Conclusions

The EIS investigations enable the effective detection of hydrogen leaks and oxygen concentrations in single cells. The conditions that may lead to internal hydrogen leakages can be identified in the simulated impedance datasets due to a slight change in the gases' partial pressure. The early detection of gas leakages is therefore a relevant safety parameter, which can be predicted on time during the operations, avoiding a potential accident scenario. Machine Learning models are undoubtedly enabling significant breakthroughs in all areas of science and technology, but often fail to describe and predict scenarios beyond the ones they have been trained on, due to a lack of knowledge on the fundamental governing laws of physical systems. Incorporating physics into ML models allows building physically consistent predictive models, which are faster to train, more generalizable, interpretable and trustworthy (Em Karniadakiset al., 2021). The predictive model based on gradient-boosted decision trees, when informed on how the current density in the internal leakage condition is related to the impedance values, can attain high reliability of correctly identifying early signals

Table 9

input features of the improved model.

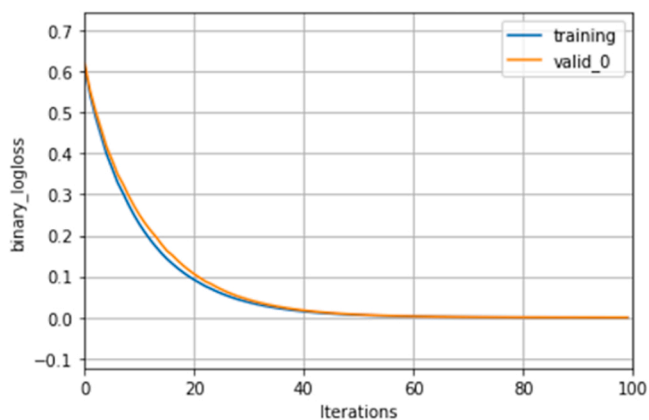| V	A	Frequency (Hz)	Z real (Ω cm²)	Z imaginary (Ω cm²)
0.65	1.482203	100000	0.154936	0.027114
0.65	1.556673	82540.42	0.157857	0.023723
0.65	1.796067	68129.21	0.160156	0.020526
0.8	1.482203	56234.13	0.161926	0.017594
1	0.794351	100000	0.170397	0.050316

Fig. 9. Errors in training and validation for the refined model.

Table 10
Refined model F-1 score.

	Precision	Recall	F-1 score	Support
Leak	0.99	0.99	0.99	79
Safe	0.99	0.99	0.99	66
Accuracy			0.99	145
Macro avg.	0.99	0.99	0.99	145
Weighted avg.	0.99	0.99	0.99	145
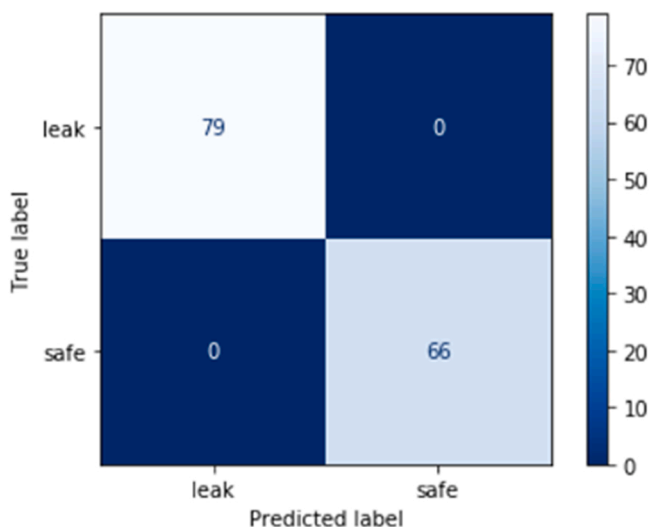
Fig. 10. Confusion matrix for the refined model.

predicting potentially hazardous situations liable to evolve towards a risk scenario.

The physics-based approach adopted in this work can be transferred to stack-sized SOFCs, thus potentially enabling the "on line" diagnosis of large-size systems for naval applications. The upscale is expected to require the optimization of the impedance execution and, in particular, the identification of the most suitable measuring parameters (e.g., frequency range, points per frequency decade, perturbation amplitude) to retain the reliability and prompt response of the approach described in this work. Further investigation on the actual capabilities of the proposed ML model are currently under development, focusing on the SOFC thermal stress and temperature profile under potential failure conditions.
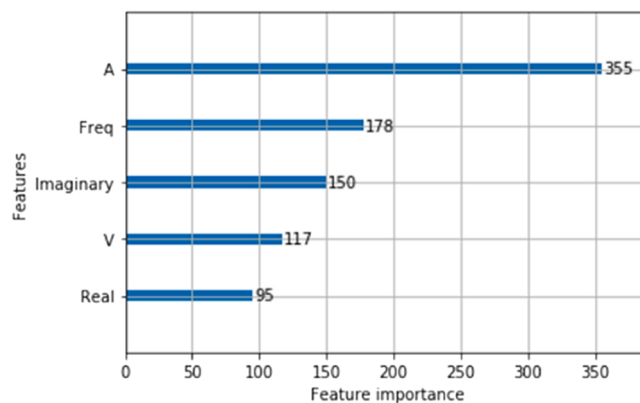

Fig. 11. Evaluation of feature importance.

Declaration of Competing Interest

The authors declare that they have no known competing financial interests or personal relationships that could have appeared to influence the work reported in this paper.

Acknowledgements

References

Aarskog, F.G., Hansen, O.R., Strømgren, T., Ulleberg, Ø., 2020. Concept risk assessment of a hydrogen driven high speed passenger ferry. Int. J. Hydrog. Energy 45 (2), 1359–1372.

Abbas, M.H., Norman, R., Charles, A., 2018. Neural network modelling of high pressure CO₂ corrosion in pipeline steels. Process Saf. Environ. Prot. 119 (2018), 36–45.

Al-Othman, A., Tawalbeh, M., Martis, R., Dhou, S., Orhan, M., Qasim, M., Ghani Olabi, A., 2022. Artificial intelligence and numerical models in hybrid renewable energy systems with fuel cells: advances and prospects. Energy Convers. Manag. 253, 115154.

Alvestad, L. Berge, K.. 2021. Handbook for Hydrogen-fuelled Vessels, DNV - MarHySafe JDP Phase 1, 1st Edition. Available at: www.iims.org.uk/wp-content/uploads/2021/07/Handbook_for_hydrogen-fuelled_vessels.pdf.

Asensio, A.M., Clematis, D., Viviani, M., Carpanese, M.P., Presto, S., Cademartori, D., Cabot, P.L., Barbucci, A., 2021. Impregnation of microporous SDC scaffold as stable solid oxide cell BSCF-based air electrode. Energy 237. https://doi.org/10.1016/j.energy.2021.121514.

Bagherzadeh, F., Nouri, A.S., Mehrani, M.J., Thennadil, S., 2021. Prediction of energy consumption and evaluation of affecting factors in a full-scale WWTP using a machine learning approach. Proc. Saf. Environ. Protec. 154, 458–466.

Baldi, F., Moret, S., Tammi, K., Maréchal, F., 2020. The role of solid oxide fuel cells in future ship. Energy Syst., Energy 194, 116811.

Bassani, A., Vianello, C., Mocellin, P., Dell'Angelo, A., Spigno, G., Fabiano, B., Maschio, G., Manenti, F., 2023. Aprioristic integration of process operations and risk analysis: definition of weighted F&EI-based concept and application to AG2S technology. Ind. Eng. Chem. Res. 62 (1), 500–510. https://doi.org/10.1021/acs.iecr.2c02289.

Bertei, A., Mertens, J., Nicolella, C., 2014. Electrochemical simulation of planar solid oxide fuel cells with detailed microstructural modeling. Electrochim. Acta 146, 151–163. https://doi.org/10.1016/j.electacta.2014.08.120.

Brokaw, R.S., 1965. Approximate formulas for the viscosity and thermal conductivity of gas mixtures. J. Chem. Phys. 42, 1140. https://doi.org/10.1063/1.1696093.

Carpanese, M.P., Clematis, D., Bertei, A., Giuliano, A., Sanson, A., Mercadelli, E., Nicolella, C., Barbucci, A., 2017. Understanding the electrochemical behaviour of LSM-based SOFC cathodes. Part I — experimental and electrochemical. Solid State Ion. 301, 106–115. https://doi.org/10.1016/j.ssi.2017.01.007.

Chen, K., Jiang, S.P., 2016. Review—materials degradation of solid oxide electrolysis cells. J. Electrochem. Soc. 163, F3070–F3083. https://doi.org/10.1149/2.0101611jes.

Chen, Y., Zhang, Y., Lin, Y., Yang, Z., Su, D., Han, M., Chen, F., 2014. Direct-methane solid oxide fuel cells with hierarchically porous Ni-based anode deposited with nanocatalyst layer. Nano Energy 10, 1–9. https://doi.org/10.1016/j.nanoen.2014.08.016.

Clematis, D., Presto, S., Carpanese, M.P., Barbucci, A., Deganello, F., Liotta, L.F., Aliotta, C., Viviani, M., 2019. Distribution of relaxation times and equivalent circuits

analysis of Ba0.5Sr0.5Co0.8Fe0.2O3−δ. Catalysts 9. https://doi.org/10.3390/catal9050441.

Eastvedt, D., Naterer, G., Duan, X., 2022. Detection of faults in subsea pipelines by flow monitoring with regression supervised machine learning. Process Saf. Environ. Prot. 161, 409–420.

Em Karniadakis, G., Kevrekidis,I.G., Lu, L., Perdikaris, P., Wang, S., Yang, L. 2021. Physics- informed machine learning, Nature Reviews – Physics, Springer Nature Ltd.

Ferrero, D., Lanzini, A., Leone, P., Santarelli, M., 2015. Reversible operation of solid oxide cells under electrolysis and fuel cell modes: Experimental study and model validation. Chem. Eng. J. 274, 143–155. https://doi.org/10.1016/j.cej.2015.03.096.

Fuller, E.N., Schettler, P.D., Giddings, J.C., 1966. New method for prediction of binary gas-phase diffusion coefficients. Ind. Eng. Chem. Res. 58, 18–27. https://doi.org/10.1021/ie50677a007.

IMO, 2017. International Code of Safety for ship using gases or other low-flashpoint fuels (IGF Code)". International Maritime Organization. https://www.imo.org/en/OurWork/Safety/Pages/IGF-Code.aspx.

Janardhanan, V.M., Deutschmann, O., 2007. Numerical study of mass and heat transport in solid-oxide fuel cells running on humidified methane. Chem. Eng. Sci. 62, 5473–5486. https://doi.org/10.1016/j.ces.2007.01.043.

Jia, C., Han, M., Chen, M., 2017. Analysis of gas leakage and current loss of solid oxide fuel cells by screen printing. E C. S Trans. 78, 1533–1540.

Jiang, Y., Virkar, A. v, 2003. Fuel composition and diluent effect on gas transport and performance of anode-supported SOFCs. J. Electrochem. Soc. (150), A942. https://doi.org/10.1149/1.1579480.

Ke, G., Meng, Q., Finley, T., Wang, T., Chen, W., Ma, W., Liu, T.-Y., 2017. Lightgbm: a highly efficient gradient boosting decision tree. Adv. Neural Inf. Process. Syst. 30, 3146–3154.

Lan, R., Tao, S., 2010. Direct ammonia alkaline anion-exchange membrane fuel cells. Electrochem Solid State Lett. 13. B83-B6.

Laosiripojana, N., Assabumrungrat, S., 2007. Catalytic steam reforming of methane, methanol, and ethanol over Ni/YSZ: The possible use of these fuels in internal reforming SOFC. J. Power Sources 163, 943–951. https://doi.org/10.1016/j.jpowsour.2006.10.006.

Li, F., Yuan, Y., Yan, X., Malekian, R., Li, Z., 2018. A study on a numerical simulation of the leakage and diffusion of hydrogen in a fuel cell ship. Renew. Sustain. Energy Rev. 97, 177–185.

Liu, M., Peng, R., Dong, D., Gao, J., Liu, X., Meng, G., 2008. Direct liquid methanol-fueled solid oxide fuel cell. J. Power Sources 185, 188–192. https://doi.org/10.1016/j.jpowsour.2008.06.076.

MEPC, 2011. MEPC Resolution 203(62). International Maritime Organization (IMO), London, United Kingdom.

Mozdzierz, M., Berent, K., Kimijima, S., Szmyd, J.S., Brus, G., 2019. A multiscale approach to the numerical simulation of the solid oxide fuel cell. Catalysts 9. https://doi.org/10.3390/catal9030253.

NAE, 2004. National Academy of Engineering, Engineering the Future, Annual Report. National Oil Spill Commission, 2011. Deep Water – The Gulf Oil Disaster and the Future of Offshore Drilling, National Commission on the BP Deepwater Horizon Oil Spill and Offshore Drilling. Washington, DC.

Osarogiagbon, A.U., Khan, F., Venkatesan, R., Gillard, P., 2021. Review and analysis of supervised machine learning algorithms for hazardous events in drilling operations. Process Saf. Environ. Prot. 147, 367–384.

Palazzi, E., Currò, F., Fabiano, B., 2020. Low rate releases of hazardous light gases under semi-confined geometry: a consequence based approach and case-study application. J. Loss Prev. Process Ind. 63, 104038.

Pasman, H.J., 2020. Early warning signals noticed, but management doesn't act adequately or not at all: a brief analysis and direction of possible improvement. J. Loss Prev. Process Ind. 104272.

Pasman, H.J., Fabiano, B., 2021. Highlights and an impression of process safety evolutionary changes from the 1st to the 16th LPS present and future of the European loss prevention and safety promotion in the process industries. Process Saf. Environ. Prot. 147, 80–91.

Pei, P., Li, Y., Xu, H., Wu, Z., 2016. A review on water fault diagnosis of PEMFC associated with the pressure drop. Appl. Energy 173, 366–385.

Petrone, R., Zheng, Z., Hissel, D., Péra, M.C., Pianese, C., Sorrentino, M., Becherif, M., Yousfi-Steiner, N., 2013. A review on model-based diagnosis methodologies for PEMFCs. Int. J. Hydrog. Energy 38, 17.

Rasmussen, J.F.B., Hendriksen, P.V., Hagen, A., 2008. Study of internal and external leaks in tests of anode-supported SOFCs. Fuel Cells 8 (6), 385–393.

Rigas, F., Amyotte, P., 2012. Hydrogen Safety. CRC Press. Taylor and Francis Group, Boca Raton, USA.

Tronstad, T., Høgmoen Åstrand, H., Haugom, G.P., Langfeldt, L 2017. DNV-GL - EMSA Study on the use of Fuel Cells in Shipping, DNV GL – Maritime 01.2017 www.emsa.europa.eu/publications/item/2921-emsa-study-on-the-use-of-fuel-cells-in-shipping.html accessed 30.11.2022.

Vairo, T., Gualeni, P., Reverberi, A.P., Fabiano, B., 2021. Resilience dynamic assessment based on precursor events: Application to ship LNG bunkering operations. Sustainability 2021 (13), 6836.

Vairo, T., Cademartori, D., Carpanese, M.P., Clematis, D., Barbucci, A., Fabiano, B., 2022. Fuel cells for shipping. An approach towards dynamic safety assessment. Chem. Eng. Trans. 90, 2022.

Valera-Medina, A., Xiaoa, H., Owen-Jones, M., David, W.I.F., Bowen, P.J., 2018. Ammonia for power. Prog. Energy Combust. Sci. 69, 63–102.

Van Biert, L., Godjevac, M., Visser, K., Aravind, P.V., 2016. A review of fuel cell systems for maritime applications. J. Power Sources 327, 345–364.

Wan, Z., Tao, Y., Shao, J., Zhang, Y., You, H., 2021. Ammonia as an effective hydrogen carrier and a clean fuel for solid oxide fuel cells. Energy Convers. Manag. 228, 113729 https://doi.org/10.1016/J.ENCONMAN.2020.113729.

Wang, Y., Li, Wenyuan, Ma, L., Li, Wei, Liu, X., 2020. Degradation of solid oxide electrolysis cells: Phenomena, mechanisms, and emerging mitigation strategies—a review. J. Mater. Sci. Technol. https://doi.org/10.1016/j.jmst.2019.07.026.

Yahya, A., Ferrero, D., Dhahri, H., Leone, P., Slimi, K., Santarelli, M., 2018. Electrochemical performance of solid oxide fuel cell: experimental study and calibrated model. Energy 142, 932–943. https://doi.org/10.1016/j.energy.2017.10.088.

Yang, X., Zhao, H., Hou, Q., 2020. Proposal and thermodynamic performance study of a novel LNG-fueled SOFC-HAT-CCHP system with near-zero CO_2 emissions. Int. J. Hydrog. Energy 45, 19691–19706. https://doi.org/10.1016/j.ijhydene.2020.05.012.

Yua, M., Pasman, H., Erraguntlac, M., Quddusa, N., Kravaris, C., 2022. A framework to identify and respond to weak signals of disastrous process incidents based on FRAM and machine learning techniques. Process Saf. Environ. Prot. 158, 98–114.

Yuanting, P., Zengshi, X., 2019. Development of hydrogen fuel cell propulsion technology for ships. Strateg. Study Chin. Acad. Eng. 21 (6), 18–21.

Zheng, Z., Petrone, R., Péra, M.C., Hissel, D., Becherif, M., Pianese, C., Yousfi Steiner, N., Sorrentino, M., 2013. A review on non-model based diagnosis methodologies for PEM fuel cell stacks and systems. Int. J. Hydrog. Energy 38, 21.